European Journal of Mechanics / A Solids 104 (2024) 105221

Contents lists available at ScienceDirect

European Journal of Mechanics / A Solids

journal homepage: www.elsevier.com/locate/ejmsol

Full length article

A multiscale finite element analysis model for predicting the effect of micro-aeration on the fragmentation of chocolate during the first bite

Georgios Samaras [a,*], Dimitrios Bikos [a], Philippa Cann [a], Marc Masen [a], Yannis Hardalupas [a], Josélio Vieira [b], Christoph Hartmann [c], Maria Charalambides [a]

[a] Department of Mechanical Engineering, Imperial College London, UK
[b] Nestlé Product Technology Centre, York, UK
[c] Nestlé Research, Lausanne, Switzerland

ARTICLE INFO

Keywords:
First human oral bite modelling
Micromechanics
Ductile fracture
Fragmentation

ABSTRACT

The emerging need to reduce the calorific value of foods, while simultaneously improving the consumer perception drives the quest for developing new food structures that satisfy both criteria. Aiming to shed light on the influence that micro-aeration has on the breakdown of chocolate during the early stages of the oral processing, this paper summarises the development of multi scale, in silico Finite Element (FE) models for the first bite. A micro-mechanical analysis was first employed to predict the impact on the mechanical properties of chocolate at two microaeration levels, i.e. f = 10vol% and f = 15vol%. The estimated elastic, plastic and fracture properties from the micromechanical model were subsequently fed into a macroscopic simulation of the first bite. Both micromechanical and the macromechanical models for the 10vol% and 15vol% porosity chocolate are compared to experimental data for validation purposes. The micromechanical models are compared to data from literature on mechanical testing of the same two chocolate materials whereas the first bite macromechanical model was compared to in vitro experimental data obtained in this study using a 3D printed molar teeth test rig mounted to a mechanical tester. Finally, the particle size distribution of the fragmented chocolate during the first bite was estimated from the in silico model and compared to in vivo literature data on the same chocolate materials and in vitro experimental data from this work. All comparisons between the in silico models and the in vitro/in vivo data led to good agreement. Our modelling methodology provides a cost-efficient tool for the investigation of new food structures that reduce the calorific value while enhancing the taste perception.

1. Introduction

Aeration is a manufacturing process widely investigated by the food industry due to efforts to achieve food structures associated with an improved consumer perception. Minor et al. (2009) stated that this change in structure retains or even enhances the original sensorial characteristics of foods. In addition, the calorific value is reduced by the decrease of the mass fraction of ingredients such as sugar and saturated fats leading to healthier products (Kokini and van Aken, 2006). Micro-aeration which introduces micron sized pores in the food material can reduce the calorific value of products such as chocolate for a given product volume, whilst at the same time it can be an important parameter for improving the sensory properties and the consumer perception. For this reason, micro-aeration is an important parameter that needs to be studied in detail. The aim of this study is to quantify the effect of micro aeration on the mechanical properties of chocolate and its behaviour during the oral process, in order to aid novel product development and optimisation.

Chocolate can be characterised as a suspension of solid particles, including cocoa particles, sugar and milk particles, in a continuous fat phase. There are different aspects that influence the oral perception of chocolates mainly involved with composition, processing operations and storage. The link between structure and compositional variations to the material properties has been reported in the literature (Afoakwa et al., 2009; Glicerina et al., 2016; Do et al., 2007; Reinke et al., 2016). Micro-aeration, even at small porosity levels, plays an important role on how the chocolate samples behave in the oral cavity. It has been shown that micro-aeration has a significant effect on material properties, such as elastic and plastic properties (Bikos et al., 2021b,a), thermal conductivity (Bikos et al., 2022b, 2023b) and friction coefficient (Samaras et al., 2020).

* Corresponding author.
E-mail address: georgios.samaras17@imperial.ac.uk (G. Samaras).

https://doi.org/10.1016/j.euromechsol.2024.105221
Received 15 May 2023; Received in revised form 30 November 2023; Accepted 1 January 2024
Available online 2 January 2024

The change in the mechanical behaviour of materials when pores are introduced in the matrix and the calculation of the effective properties is performed through the theory of computational homogenisation. Computational homogenisation is often used to derive the effective properties of heterogeneous materials, by knowing the properties of their constituents. Homogenisation can also be applied for non-linear properties and it has been the field of research in many papers e.g. Michel and Suquet (1992), Castañeda (1991), Castaneda (2002). In the current paper, homogenisation will be used for porous chocolate, where the air will be considered as the second phase of the heterogeneous material. The theory of computational homogenisation will be applied to random porous microstructures, which will be developed through a Random Sequential Adsorption (RSA) algorithm (Rintoul and Torquato, 1997) and to geometries generated from 3D reconstruction of X-ray Tomography (XRT) images. The study on the random microstructure aims to provide the geometric characteristics in terms of size and number of pores, which is sufficient to represent the macroscopic properties. This statistically homogeneous unit cell is known as the Representative Volume Element (RVE) and it will be used for the computational homogenisation.

Modelling of fragmentation during the first bite is highly influenced by the chosen damage framework. The local Continuum Damage Mechanics (CDM) models suffer from mesh dependent results and the damage parameter tends to increase with increasing mesh refinement (Dorgan, 2006). This is a result from the loss of ellipticity of the governing differential equations (Aravas and Papadioti, 2021). The absence of an internal material length in the classical continuum theory, causes the characteristic element length to become the material length. This limitation can be overcome by using non-local models (Aifantis, 1984a). In non-local models, an additional internal material length variable is introduced that takes into account the influence of the surrounding neighbourhood at each material point (Aifantis, 1984b). The non-local models have been extensively used in the context of porous metal plasticity (Leblond et al., 1994; Enakoutsa, 2014; Reusch et al., 2003; Jackiewicz and Kuna, 2003) but have not been applied before when studying food fragmentation.

In the field of oral processing, Harrison and Cleary (2014), Harrison et al. (2014) used a coupled bio- mechanical-smoothed particle hydrodynamics (bSPH) model that predicts the food breakdown due to the interaction of the food with saliva and anatomical structures of the mouth (tongue, teeth, cheeks). Although this study takes into account a more accurate scenario where the food interacts with more surfaces in the mouth, the constitutive model used was a simple elastic-perfectly plastic model coupled with a simple fracture criterion. Dejak et al. (2003) presented an FE model to analyse the stresses induced by the molar teeth during chewing of morsels using various elastic moduli. Skamniotis et al. (2016) demonstrated an FE model in the ABAQUS/Explicit solver that simulates the first bite of pet food. In this model a more sophisticated viscoplastic material model was used coupled with a ductile damage evolution law that is driven by the fracture toughness. The results of this study were promising although a local damage model was used, making the simulation results mesh dependent.

The aim of the present study is, hence, to provide a multiscale analysis that takes into account a microstructural change (porosity) and quantifies the effect on the fragmentation during the first bite. More specifically, the multiscale model assumes that the solid matrix of the two micro-aerated samples (f = 10vol% and f = 15vol%) has the same properties as the non aerated chocolate, and estimates the change in the mechanical properties due to the pores. Moreover, these properties are used as input for a macroscale *in silico* model of the first bite, where a non local damage model is applied. The *in silico* model is validated against an *in vitro* laboratory replicate of the first bite. Finally, the fragments obtained from the *in vitro* and *in silico* models are compared against already available *in vivo* mastication results (Bikos et al., 2021b). Overall, the multiscale model of the present paper can be used in two ways; initially, the micromechanical analysis can be used to investigate how the change in structure affects the mechanical properties, and the macroscale model can provide a reliable prediction of fragmentation size that is itself related to the consumer perception (Di Monaco et al., 2014; Cheong et al., 2014).

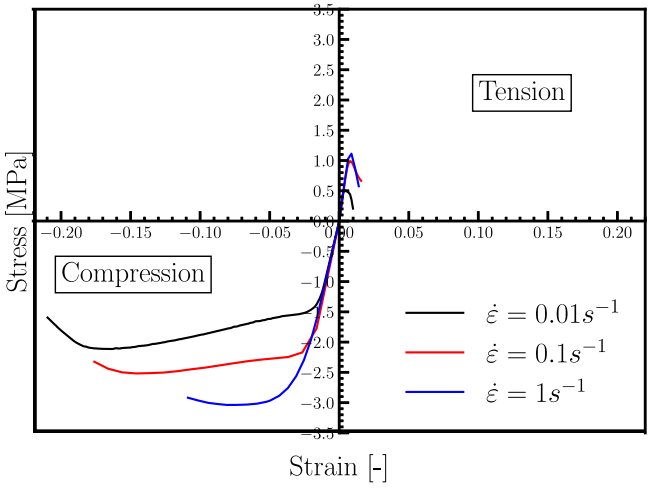

Fig. 1. Compression and tension experimental true stress versus true strain data for non aerated chocolate. Data adopted from the study of Bikos et al. (2021b), Bikos (2022). The experimental data correspond to three different true strain rates $\dot{\varepsilon} = 0.01, 0.1$ and $1\,s^{-1}$.

2. Materials and methods

2.1. Materials

The chocolate samples were provided by the Nestlé- Product Technology Centre (NPTC) in York, UK and were also used in the study of Bikos et al. (2021b) who tested the measured the mechanical properties. The chocolate samples had a typical composition of 44 wt% sugar particles, 27 wt% cocoa fat, 10 wt% whole milk powder, 6 wt% non-fat cocoa solids, and 0.3% sunflower lecithin. Three chocolate materials were provided with 0 vol%, 10 vol% and 15 vol% microaeration levels.

The tensile and compressive experimental data of true stress versus true strain for three true strain rates are shown in Fig. 1 for the non aerated (f = 0vol%) chocolate. The data showed small variations and the error bars were very small (Bikos et al., 2021b; Bikos, 2022). The compressive and tensile stress–strain behaviour of the two micro-aerated chocolate materials were also available in Bikos et al. (2023a) and are presented here in Figs. 8(a) and 9(a) where comparisons are made with the micromechanical models in Section 3.

2.2. Microstructure of micro-aerated samples

The microstructure of both micro-aerated and non micro-aerated (f = 0vol%) samples was investigated though the Scanning Electron Microscope (SEM). Figs. 2a and 2b show the microstructure of the two chocolate materials, f = 0vol% and f = 15vol% respectively. Besides pores, which are clearly seen in Fig. 2b, sugar particles are also visible. The sugar particles appear as crystals and their size ranges between 10 μm to 40 μm (Bikos et al., 2021b), which is in agreement with values reported in the literature (Reinke et al., 2016). The pore size distribution from these SEM images is shown in Fig. 3(a).

In order to further investigate the microstructure of the micro-aerated samples, XRT was also taken (Bikos et al., 2021b) and the average pore size distribution was calculated (Fig. 3(a)). The 2D SEM images led to an average pore diameter of 38 μm and the average pore diameter calculated through the 3D XRT image was 45 μm for

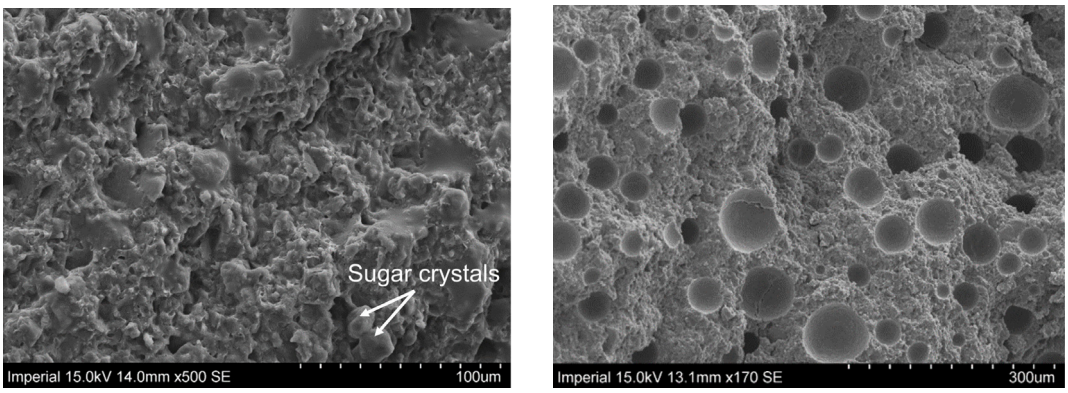

Fig. 2. SEM images of (a) non micro-aerated and (b) f = 15vol% micro-aerated samples. More details about the SEM images and additional information appearing in them, e.g. sugar crystals, can found in the paper published by Bikos et al. (2021b).

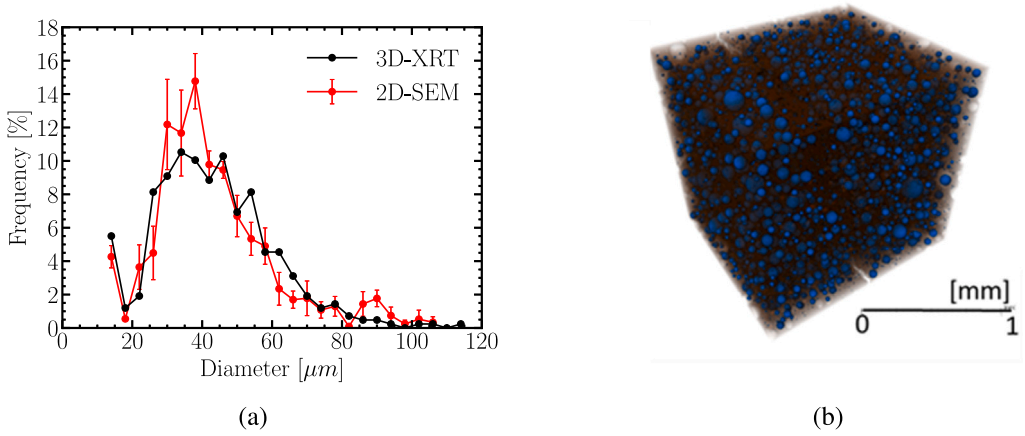

Fig. 3. (a) Size distribution of pores measured from five SEM images (in the case of the f = 10vol% and f = 15vol% chocolate) and 3D geometry from XRT images (only f = 15vol% chocolate), (b) 3D representation based on XRT images showing the pores dispersed inside the f = 15vol% micro-aerated chocolate, the blue spheres, i.e. micro-pores are randomly dispersed into the brown cube, i.e. chocolate 3D contour plot of the pore diameters processed from the XRT images (Bikos et al., 2021b). (For interpretation of the references to colour in this figure legend, the reader is referred to the web version of this article.)

both micro-aerated samples with f = 10vol% (results not shown) and f = 15vol% micro-aeration (Bikos et al., 2021b). The latter mean value of 45 μm was used for the generation of monodisperse and polydisperse virtual porous geometries for the micromechanical study, as will be described in Section 3. The actual 3D reconstructed geometry from XRT, shown in Fig. 3(b), was also used in the micromechanical study in addition to the generated virtual porous unit cells. This analysis will be presented in detail in Section 3.

Fig. 3(a) reveals that a few bigger pores of diameter higher than 100 μm are present in the aerated samples. These bigger pores were also present in the non-aerated chocolate, due to the manufacturing process. The bigger pores were hence not included in the micro-mechanical study.

2.3. Experimental in vitro replicate of the first bite

A pair of upper and lower molar teeth were extracted from a digitised adult male 3D skull, generated using X-ray tomography, and were used for both the *in vitro* experimental rig and the *in silico* FE simulations. The two sets of molar teeth were tilted in order to become normal to the laboratory surface and also to simplify the model. In order to attach the molar teeth onto a screw driven mechanical tester, adaptors were designed and were 3D printed as one continuous piece with the teeth using a Stratasys Dimension 1200es machine and were made of Acrylonitrile Butadiene Styrene (ABS). A compliance test was also employed to eliminate any effects that a possible deformation of the ABS has due to interaction with the chocolate and also correct for the compliance of the machine. For a more detailed description of the experimental rig, the reader is referred to the study of Samaras et al. (2023). The chocolate specimens were cut using a razor blade in lengths of 10 mm. The width of 14 mm and height of 8 mm was fixed from the manufacturing process of the specimens and the overall cross sectional area was 140 mm^2. These dimensions correspond to a mass of 1.5 g, which is consistent with the study of Lucas and Luke (1983) and in the range of the mouthful size (Chen, 2009; Yven et al., 2010). Fig. 4 depicts the 3D printed molar teeth together with the chocolate specimen.

2.4. Particle size distribution of fragments from in vivo and in vitro models of the first bite

The *in vivo* mastication tests were conducted by five volunteers, who were asked to chew the chocolate specimens for one cycle (Bikos et al., 2021b). The chocolate specimens were cut using a razor blade in lengths of 10 mm. The width of 14 mm and height of 108 mm was provided from the manufacturing process of the specimens and overall the cross sectional area was 140 mm^2. The specimens were placed in thin plastic sealed bags of 0.02 mm thickness, to avoid the contact of the specimens with the saliva and the inner mouth surfaces. Isolating the food specimen using sealed bags, allows for the study of fragmentation

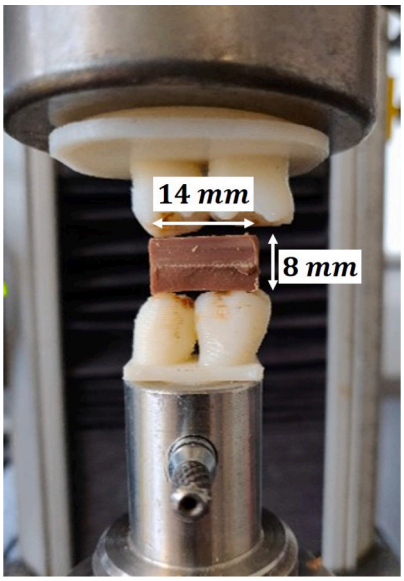

Fig. 4. Experimental set up consisting of the 3D printed teeth attached to a screw driven mechanical tester. The position and the dimensions of the chocolate sample are also shown.

due to the interaction with the teeth without considering the chemical degradation and hydration of the chocolate due to interactions with the saliva. The silicon bags also facilitated the collection of the fragments after the end of each mastication test. The volunteers were asked to place the bag with the specimen between the molar teeth and chew naturally; no further instruction was given regarding the applied force or the speed that they would apply to perform the bite. Afterwards, the plastic sealed bags were collected, the fragments were removed from the bags, dropped gently onto a flat plate and a colour image was captured. The methodology presented by Bikos et al. (2021b) for the estimation of the fragmentation is briefly presented here. The morphology of the fragments was studied through image analysis techniques (Yven et al., 2010) using the open source software ImageJ (v1.52 National Institutes of Health) (Schneider et al., 2012). The colour images were imported into ImageJ, where the image contrast was changed in order to make the edges of the fragments more visible and the different fragments more distinct. The images were then turned into 8-bit format (black and white) and the process for calculating the 2D area covered by the fragments was enabled. The surface area covered by the fragments was converted to an equivalent diameter corresponding to the same area. Based on these diameters, the size distribution was computed and averaged across the five volunteers. The methodology developed by Sahagian and Proussevitch (1998) was applied to convert the 2D diameter distribution into a 3D size distribution. This approach takes into account any random cut plane and any shape of particles to convert the 2D size distribution into a 3D distribution and therefore to correct any errors associated with the naturally fractured 2D surfaces.

The same procedure as above was also followed for the in vitro mastication where the experiment presented in Section 2.3 was repeated with food specimens in silicon bags. The effect of the silicon bags on the force–displacement curves was investigated by comparing the force–displacement curves with and without the silicon bags present. It was found that the results were not influenced by the presence of the silicon bag and the force–displacement measurement with the silicon bag lied in the error bar range of the values obtained without the silicon bags. The same methodology was followed for the estimation of the fragment particle size distribution. This enabled the comparison between the in vivo and in vitro fragmentation of the chocolate due to the first bite.

3. Micromechanical modelling

The micro-aerated chocolate consists of a polydisperse porous distribution in the matrix. In this section, the methodology followed to estimate how the elastic, plastic and fracture properties are influenced by micro-aeration is presented. Initially, the size of the unit cell that can be considered as representative is calculated and then FE simulations are employed to estimate the mechanical properties for the two porosity levels, $f = 10\text{vol}\%$ and $f = 15\text{vol}\%$, for both monodisperse and polydisperse pore distributions. Finally, the analytical models used to compare the experimental and computational results are presented.

3.1. Generation of virtual microstructures

The open source code Mote3D (Richter, 2017) is a Random Sequential Adsorption (RSA) algorithm capable of generating random particulate microstructures with periodic surfaces and it was used for the generation of both monodisperse and polydisperse porous microstructures with micro-aeration levels $f = 10\text{vol}\%$ and $f = 15\text{vol}\%$. The following parameters needed to be specified in Mote3D: the edge length of the cube, the number of voids (spherical particles), the mean and standard deviation (for polydisperse distribution) of the voids' diameter distribution and the particle overlap factor that defines the minimum acceptable distance between adjacent particle centres (Richter, 2017). Representative porous microstructures of increasing volume, but constant micro-aeration level of $f = 15\text{vol}\%$, are depicted in Fig. 5.

Mote3D gave outputs of the centre coordinates and radii of the pores. These data were then processed by a Python script to generate a readable file by the commercial software NETGEN (Schöberl, 1997) which was used for meshing the microstructures. NETGEN (Schöberl, 1997) is capable of creating periodic meshes, which is required in the current study, by creating identical surface meshes at opposite surfaces of the unit cell. The unit cells were meshed with three dimensional ten-node quadratic tetrahedral elements (C3D10 in ABAQUS Michael, 2017).

3.2. Boundary conditions and estimation of RVE size

Following the study of Zerhouni et al. (2019), the size of the RVE was calculated by comparing the behaviour of the generated RVEs when Kinematic Uniform Boundary Conditions (KUBC) and Periodic Boundary Conditions (PBC) are applied. Eq. (1) describes the KUBC, where an average strain $\bar{\varepsilon}$ is applied at any material point $\mathbf{x}$ of the boundary of the unit cell ∂V and the displacement field $\mathbf{u}(\mathbf{x})$ is:

$$\mathbf{u}(\mathbf{x}) = \bar{\varepsilon} \cdot \mathbf{x} \tag{1}$$

KUBC overconstrain the unit cell providing an overestimation of the effective elastic properties. PBC are imposed on the opposite boundaries of the unit cell as described by Mbiakop et al. (2015) and the displacement field $\mathbf{u}(\mathbf{x})$ is given by:

$$\mathbf{u}(\mathbf{x}) = \bar{\varepsilon} \cdot \mathbf{x} + \mathbf{u}^*(\mathbf{x}) \tag{2}$$

where $\mathbf{u}^*(\mathbf{x})$ is a periodic field. The PBC were applied in ABAQUS (Michael, 2017) through an MPC subroutine provided from the NETGEN (Schöberl, 1997) open source software used to mesh the unit cells.

The convergence criterion introduced by Zerhouni et al. (2019) was used to estimate the size of the unit cell that can be considered as representative of the whole volume. This states the following:

- the difference between the effective properties calculated by applying KUBC and PBC should be less than 2% and
- further increase of the size of the unit cell does not fluctuate the effective properties calculated by KUBC by more than 0.1%

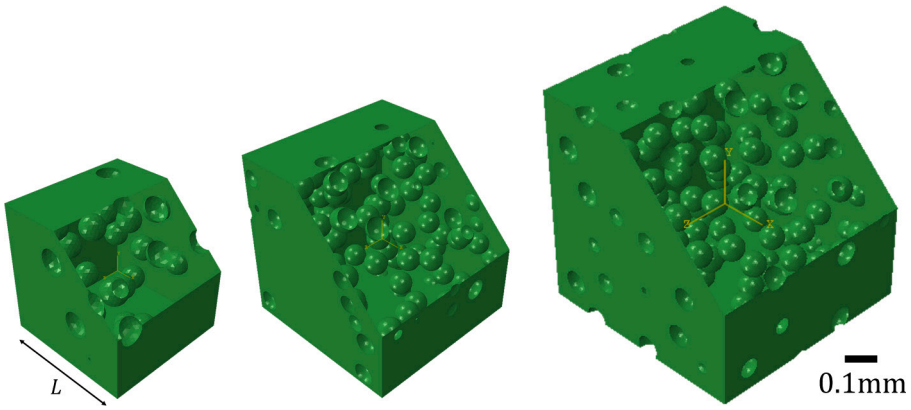

Fig. 5. Unit cells of $f = 15$vol% micro-aeration, generated with the RSA algorithm. The increasing size of the cubes is accommodated with increased number of pores in order for the porosity to remain constant.

Table 1
Sizes of unit cells, for the two examined porosities, used for the computation of RVE. The sizes correspond to both monodisperse and polydisperse microstructure, and the radius (mean radius for the polydisperse unit cells) is $R = 22.5\,\mu$m.

	$f = 10$vol%	$f = 15$vol%
N	L [mm]	L [mm]
30	0.24	0.21
50	0.28	0.25
75	0.32	0.28
100	0.36	0.31
150	0.42	0.36

The PBC is the most efficient in terms of the convergence rate with increasing RVE size, whereas the KUBC provides a wrong prediction of the effective property for small RVEs and converges to an asymptotic value of the averaged property for bigger volumes. The convergence of apparent properties to the effective ones as the size of the unit cell increases, has been investigated by Huet (1990, 1999), Ostoja-Starzewski (1998, 1999), Pecullan et al. (1999) and Terada et al. (2000).

Four different sizes of periodic unit cells with gradually increasing size of edge length L and number of pores N (to keep the porosity constant) were examined for both porosities of $f = 10$vol% and $f = 15$vol%. Detailed information about the unit cells generated with the RSA algorithm is presented in Table 1. Micromechanical analysis is also conducted on the 3D reconstructed geometry of Fig. 3(b) and since the geometry is not periodic, only KUBC are applied on the boundaries.

The two types of boundary conditions presented above were implemented to the generated microstructures and linear elastic FE simulations were conducted, where the matrix was modelled as a linear isotropic material with Young's modulus $E = 100$ MPa and Poisson's ratio $\nu = 0.49$, which are properties calculated from experiments conducted on the non-aerated chocolate samples. More details regarding the experimental procedure can be found in the work of Bikos et al. (2021b). The estimation of the representative volume size was made under the linear elastic assumption, in order to reduce the computational time. A more accurate constitutive model was applied for the estimation of the plastic and fracture properties.

The homogenised stiffness tensor is calculated from the volume average stress and volume average strain fields using the constitutive equation:

$$\overline{\boldsymbol{\sigma}}(\mathbf{x}) = \mathbb{C}^{eff} : \overline{\boldsymbol{\varepsilon}}(\mathbf{x}) \tag{3}$$

where $\mathbb{C}^{eff}$ is the effective stiffness tensor.

According to Kanit et al. (2003) the homogenised stiffness tensor is calculated by imposing six average strain fields in different directions in order to calculate all the six columns of $\mathbb{C}^{eff}$. Taking advantage of the isotropic behaviour of the microstructures developed using the RSA algorithm (Anoukou et al., 2018), the elastic properties can be described by the bulk modulus, k, and the shear modulus, μ. The reader is referred to the study of Kanit et al. (2003) for a detailed description of the methodology.

3.3. Material modelling

A modified Johnson-Cook constitutive model without the effect of temperature was employed to model the chocolate in the RVEs of the micromechanical models. Eq. (4) describes the constitutive equation:

$$\sigma_y = \left[A + B\left(\varepsilon^p_{eq}\right)^n\right]\left[1 + C\ln\left(\frac{\dot{\varepsilon}^p_{eq}}{\dot{\varepsilon}_0}\right)\right] \tag{4}$$

where ε^p_{eq} is the equivalent plastic true strain, $\dot{\varepsilon}^p_{eq}$ is the equivalent plastic true strain rate, $\dot{\varepsilon}_0$ is the reference strain rate ($0.01\,\text{s}^{-1}$ in Fig. 1) which corresponds to the lowest strain rate the experiments were conducted. The parameters A, B and n control the hardening behaviour and the terms C and $\dot{\varepsilon}_0$ the rate dependent behaviour. The Young's modulus, E, and the Poisson's ratio, ν, was taken from the study of Bikos et al. (2021b). It is noteworthy that the Johnson-Cook constitutive model has demonstrated successful application to non-metallic materials such as concrete (Wan et al., 2021), which, like chocolate (Bikos et al., 2023a), are granular particulate systems. Furthermore, considering that chocolate is a highly filled material comprising crystalline particles such as sugar and fat, there exists a phenomenological resemblance to behaviours observed in metallic materials. The compression data in Fig. 1 were used to calibrate the Johnson-Cook model, as this allowed calibration to higher strains. The tensile experimental data were however employed for the definition of the plastic strain at fracture as a function of the triaxiality factor. During the first bite process, the teeth apply compressive loads hence the compression data are important. However, it is argued that fracture occurs due to the lateral tensile deformation, hence the fracture data in tension are also needed. The Young's modulus, E was estimated from the compressive experimental data of Fig. 1 and was considered the same for tension. It is worth noting that, the elastic modulus in compression for the strain rates used for calibration ($\dot{\varepsilon} > 0.01\,\text{s}^{-1}$) was constant (Bikos et al., 2021b) and the viscoelastic behaviour was ignored taking into account only the rate-dependent plastic response through the Johnson-Cook constitutive model. All the calibrated parameters are given in Table 2. The Johnson-Cook model was implemented in ABAQUS through a VUMAT subroutine in order to be coupled with a VDFLUX subroutine as it will be discussed in Section 3.3.2. In the current study, the assumption that the mouth temperature does not influence the fragmentation of the food during the first bite is being

Table 2
Material properties for non aerated chocolate for the FE simulations.

Parameter	Value
Density, ρ [kg m^{-3}] (Bikos et al., 2021b)	1300
Elastic modulus, E [MPa]	100
Poisson's ratio, ν [–]	0.49
A [MPa]	1.35
B [MPa]	3.5
C [–]	0.05
n [–]	0.8
$\dot{\epsilon}_0$ [s^{-1}]	0.01
Internal length, l [mm]	0.08
d_{cr}	0.1

Table 3
Equivalent plastic strain at damage onset for non aerated chocolate for different stress states and strain rates.

$\epsilon^p_{eq,i}$	η	$\dot{\epsilon}$(s^{-1})
0.16	−1/3	0.01
0.0058	0	0.01
0.006	1/3	0.01
0.154	−1/3	0.1
0.0069	0	0.1
0.008	1/3	0.1
0.08	−1/3	1
0.0078	0	1
0.009	1/3	1

made. Furthermore, in both micromechanical and micromechanical simulations where the non local damage model is applied, temperature is used through a VDFLUX subroutine but has no physical meaning. Moreover, it is important to note that the low thermal conductivity and relatively high specific heat capacity of chocolate can act as limiting factors that inhibit self-heating (Bikos et al., 2023b).

3.3.1. Ductile damage model

Although several damage models exist in the literature (Le et al., 2018), a version of the modified damage model of Bai and Wierzbicki (2008) is adopted in the current study. For a direct comparison with the built-in ductile damage model of ABAQUS, the same linear dissipation-energy-based damage evolution law is applied (Michael, 2017), and the rate of evolution of the damage parameter, $\dot{d}$, is given by:

$$\dot{d} = \frac{\sigma_{y,i} l}{2G_f}\dot{\epsilon}^p_{eq} \tag{5}$$

where $\sigma_{y,i}$ is the yield stress at the damage onset, l is an internal length, $\dot{\epsilon}^p_{eq}$ is the equivalent plastic strain rate, and G_f is the fracture energy with dimensions of energy per unit surface area [J/m^2]. Overall the damage evolution law is controlled by a damage initiation equivalent plastic strain, $\epsilon^p_{eq,i}$ and an energy based evolution law including the triaxiality parameter, η:

$$d = \begin{cases} 0; & \epsilon^p_{eq} \le \epsilon^p_{eq,i} \\ \int_{\epsilon^p_{eq,i}}^{\epsilon^p_{eq,f}} \frac{\sigma_{y,i} l}{2G_f}\, \mathrm{d}\epsilon^p_{eq}; & \epsilon^p_{eq,i} < \epsilon^p_{eq} < \epsilon^p_{eq,f} \\ d_{cr} & \epsilon^p_{eq} = \epsilon^p_{eq,f} \end{cases} \tag{6}$$

where complete damage is achieved when the damage parameter d reaches a critical value d_{cr}. The G_f value of the chocolate was reported to be in the range 8–12 J/m^2 (Bikos et al., 2021b) for the different speeds and an average value of $G_f = 10$ J/m^2 is adopted for the damage evolution law of Eq. (6). The internal length and the critical damage value are calibrated following the methodology presented in the study of Wu et al. (2017), were found to be $l = 0.08$ mm and $d_{cr} = 0.1$ respectively (Samaras et al., 2023). Table 2 summarises the calibrated parameters of the constitutive and damage models.

The compressive and tensile experimental data were used for the estimation of the equivalent plastic strain at fracture initiation, $\epsilon^p_{eq,i}(\dot{\epsilon}, \eta)$. The maximum points in the compressive part of the stress–strain data in Fig. 1 were used as the value of $\epsilon^p_{eq,i}$ for compression ($\eta = -1/3$). For tension, $\eta = 1/3$, the maximum points in the tensile stress–strain data were used. In both cases, the value of $\epsilon^p_{eq,i}$ was given as a function of applied true strain rate, $\dot{\epsilon}$. The damage criterion was extended to include the equivalent plastic strain in shear, $\epsilon^{p,s}_{eq,i}$, for each strain rate $\dot{\epsilon}$ as well. The equivalent plastic strain in shear ($\eta = 0$) is approximated using Eq. (7) (Skamniotis et al., 2017) derived from the von Mises equivalent strain, with $\epsilon^{p,t}_{eq,i}$ representing the equivalent plastic strain at the damage onset in tension.

$$\epsilon^{p,s}_{eq,i} = \frac{\sqrt{3}}{2}\epsilon^{p,t}_{eq,i} \tag{7}$$

The equivalent plastic strains for non aerated chocolate at the damage onset for different strain rates and stress triaxiality values are shown in Table 3. It is important to acknowledge that the stress triaxiality values in both the micromechanical and first bite models extend beyond the calibrated range of −1/3 to +1/3. This specific range was chosen to replicate the experimental conditions, particularly in compression and tension tests, which served as the basis for calibrating the constitutive model. In cases where the stress triaxiality values fall outside this calibrated range, Abaqus extrapolates to estimate these values (Michael, 2017).

3.3.2. Strain gradient enhanced damage model

Peerlings et al. (1996) formulated the implicit gradient form of the Pijaudier-Cabot and Bažant (1987) non-local approach, which is written as:

$$e^p_{eq} - l_{ch}\nabla^{(2)} e^p_{eq} = \epsilon^p_{eq} \quad \text{in} \quad \Omega \tag{8}$$

where ϵ^p_{eq} is the local equivalent plastic strain, e^p_{eq} is the non-local equivalent plastic strain, l is the internal characteristic length with dimensions of length and Ω is the occupied domain. Eq. (8) is solved together with the following natural boundary condition.

$$\frac{\partial e^p_{eq}}{\partial n} \equiv \mathbf{n}\cdot\nabla e^p_{eq} = 0 \quad \text{on} \quad \partial\Omega \tag{9}$$

where $\mathbf{n}$ is the unit outward normal vector to the surface $\partial\Omega$. Eq. (8) defines the non-local equivalent plastic strain implicitly in terms of the local plastic strain and together with the boundary condition of Eq. (9) formulate the boundary value problem that needs to be solved.

Eqs. (8) and (9) were solved following the work of Papadioti et al. (2019), who took advantage of the similarities between Eq. (8) and the transient heat transfer equation given by:

$$k\nabla^{(2)} T + r = \rho c\dot{T} \tag{10}$$

where c is the specific heat, T is the temperature, k is the thermal conductivity, r is the heat supply per unit volume and ρ is the density (Michael, 2017). Comparing Eqs. (8) and (10) there is a direct correlation between the non-local equivalent plastic strain, e^p_{eq}, and the temperature, T. It is, then, possible to use the already available VDFLUX subroutine in ABAQUS Explicit (Michael, 2017), to solve the non-local problem, by replacing T with e^p_{eq}, k with l_{ch} and finally r with $\epsilon^p_{eq} - e^p_{eq}$ (Samaras et al., 2023).

The transient heat transfer Eq. (10) is already implemented in the VDFLUX subroutine which can be coupled with the constitutive equations in the VUMAT. The l_{ch} was calculated by performing benchmark tests similar to Seupel et al. (2018). In those benchmark tests where an induced shear band was formed, the l_{ch} was selected so the width of the shear remained constant for different mesh refinements. The l_{ch} is a geometrical parameter and depends on the size of the specimen. In the current paper, the value selected for the micro-mechanical and macro-mechanical *in silico* model will be defined in Sections 4 and 5.2. The reader is referred to the study of Papadioti et al. (2019) for a detailed

discussion regarding the computational aspects that should be taken into account when using the transient heat transfer equation to solve Eq. (8). The efficacy of the strain gradient enhanced damage model on reducing the mesh dependency of the results has been presented in our recently published paper (Samaras et al., 2023), where different mesh refinements of the food sample in the first bite model has been employed. A coarse (100,000 elements) and a dense (140,000 elements) mesh discretisation of the food specimen was applied and the force–displacement data were compared. It was found that the non-local damage law implemented through the VDFLUX subroutine alleviates the model from mesh-dependent results that were present when the local damage model was applied.

3.4. Analytical models

The Hashin–Shtrikman (HS) upper bound and Voigt bound are used for determining the Young's modulus for comparison with the numerical and experimental results. The Young's modulus, according to the Voigt model is calculated as follows:

$$E_i = fE, \quad i = \{10\,\text{vol\%}, 15\,\text{vol\%}\} \tag{11}$$

where E is the Young's modulus of the non aerated chocolate, E_i is the Young's modulus of the porous chocolate (10vol% or 15vol%) and f is the porosity.

Hashin and Shtrikman (1963) extended the Voigt and Reuss models and provided closer upper and lower bounds for the elastic modulus. The bulk, k_{HS}, and shear, μ_{HS}, moduli according to the Hashin–Shtrikman upper bounds are calculated as:

$$k_{HS} = \frac{4(1-f)\mu_m k_m}{4\mu_m + 3fk_m} \tag{12}$$

$$\mu_{HS} = \frac{(1-f)\left(8\mu_m + 9k_m\right)\mu_m}{4\mu_m(2+3f) + 3k_m(3+2f)} \tag{13}$$

where k_m and μ_m are the bulk and shear moduli of the matrix. The Young's modulus, E, and the Poisson's ratio, ν, are then calculated using the following equations:

$$E_{HS} = \frac{9k_{HS}\mu_{HS}}{3k + \mu_{HS}} \tag{14}$$

$$\upsilon_{HS} = \frac{3k_{HS} - 2\mu_{HS}}{6k + 2\mu_{HS}} \tag{15}$$

The two analytical models will be compared against the results from the micromechanical analysis and the experimental data.

4. Micro-mechanical model results

Initially, the results for the prediction of the elastic modulus are presented, where simulations using both the monodisperse and the polydisperse pore distributions were conducted. The error bars, presented in the figures of this section, correspond to the maximum and minimum values calculated using five different RVE configurations randomly generated by Mote3D. In Figs. 6(a) and 6(b), the normalised Young's moduli of the $f = 10$vol% chocolate for various monodisperse and polydisperse configurations are presented respectively. The PBC converge faster than the KUBC, as expected, and the error bars of the calculations are smaller for the PBC. The normalised Young's modulus with PBC reaches a constant value for unit cell with $N = 75$ pores, whereas the KUBC converge for a larger unit cell of $N = 100$ pores. The convergence criteria are met for both KUBC and PBC for a unit cell with $N = 100$ pores, mean diameter of $D = 45\,\mu$m and edge size of $L = 0.36$ mm. This is in agreement with the findings of Zerhouni et al. (2019) who suggested that a ratio of $D/L \approx 0.1$ leads to converged RVEs. The normalised Young's moduli of the $f = 15$vol% chocolate for monodisperse and polydisperse microstructures are presented in Figs. 6(c) and 6(d) respectively. The results showed that a unit cell with $N = 100$ pores and edge size $L = 0.31$ mm is considered as representative.

The elastic modulus results from the micromechanical models for both porosities $f = 10$vol% and $f = 15$vol% are presented in Fig. 7. In the same Figure, the normalised Young's modulus from the upper Hashin Shtrikman bound and the Voigt model is shown for comparison purposes. In addition, experimental data on the same chocolate materials taken from Bikos et al. (2021b) are also added in Fig. 7. An excellent agreement is observed between the FE models and the experimental data. The two analytical models are also close to the FE model results and the experimental data. The XRT geometry for porosity $f = 15$vol%, was also modelled in FE and the calculated Young's modulus lies between the error bars of both experiments and FE simulations using the MOTE3D generated geometries. It is worth mentioning that although KUBCs were used in the XRT, which overestimate the effective properties, the results agree with those of the converged RVEs, where PBC were used. This result is reasonable, since, as shown in Fig. 3(b), the size of the XRT geometry ($L_{XRT} > 1$ mm) is greater than the size of the RVE ($L_{RVE} = 0.31$ mm), which was selected according to the convergence criteria, and the effective properties calculated with KUBC coincide with the PBC for large RVE sizes.

The converged RVE microstructures, as determined from the elastic analysis, were used for the estimation of plastic and fracture properties of the micro-aerated chocolate. The lower surface of the RVEs was encastred whereas the tensile or compressive displacement was applied at the top surface. This type of boundary conditions allowed the direct comparison of the FE simulations to the experimental data. The constitutive model coupled with the non-local damage evolution law was used in compression and tension FE simulations for different strain rates using the converged RVE geometries. Different mesh refinements were tested for both the polydisperse and the monodisperse microstructures, and the value of $l_{ch} = 0.06$ mm provided mesh-independent results without making the FE simulations computationally expensive. The stress–strain curves from the FE simulations were compared with compression and tension experiments. The purpose of this analysis was to study the effect of the pore distribution on the mechanical properties through a comparison between monodisperse and polydisperse unit cells.

Both monodisperse and polydisperse microstructures were modelled for both porosities. All results exhibited a small variation, less than 5%, in their mechanical response over the five repeats for all testing rates. Therefore, the error bars are very small and not shown for clarity in Figs. 8(a), 8(b), 9(a) and 9(b). The stress–strain graph for tension and compression for porosity $f = 10$vol% with polydisperse distribution is presented in Fig. 8(a). The respective data of the monodisperse distribution of the same porosity is shown in Fig. 8(b). Comparing Figs. 8(a) and 8(b), initially, the elastic region in the compressive loading of the FE simulations is in good agreement with the experimental data and no difference is observed between monodisperse and polydisperse configurations. The FE simulations were also capable of capturing the initial yield stress for both distributions and lie in good agreement with the experimental data. Differences between polydisperse and monodisperse microstructures appear in the plastic region. The fracture initiation criterion was met at smaller strains for the monodisperse configuration resulting in softening to occur faster leading to failure at smaller strains than the experiments and the polydisperse pore configuration. This is not present in the polydisperse configurations, where the stress–strain graph of Fig. 8(a) reveals a more ductile behaviour resulting in a plastic region and final a fracture strain that is in good agreement with the compression experiments. A similar effect is also present in the tensile stress–strain data. The polydisperse distribution is in better agreement with the experiments than the monodisperse RVEs.

The same analysis was performed for the $f = 15$vol% for both monodisperse and polydisperse microstructures. A similar trend to the $f = 10$vol% is also present for the $f = 15$vol% as shown in Fig. 9. In compression, the yield point is captured correctly for both polydisperse

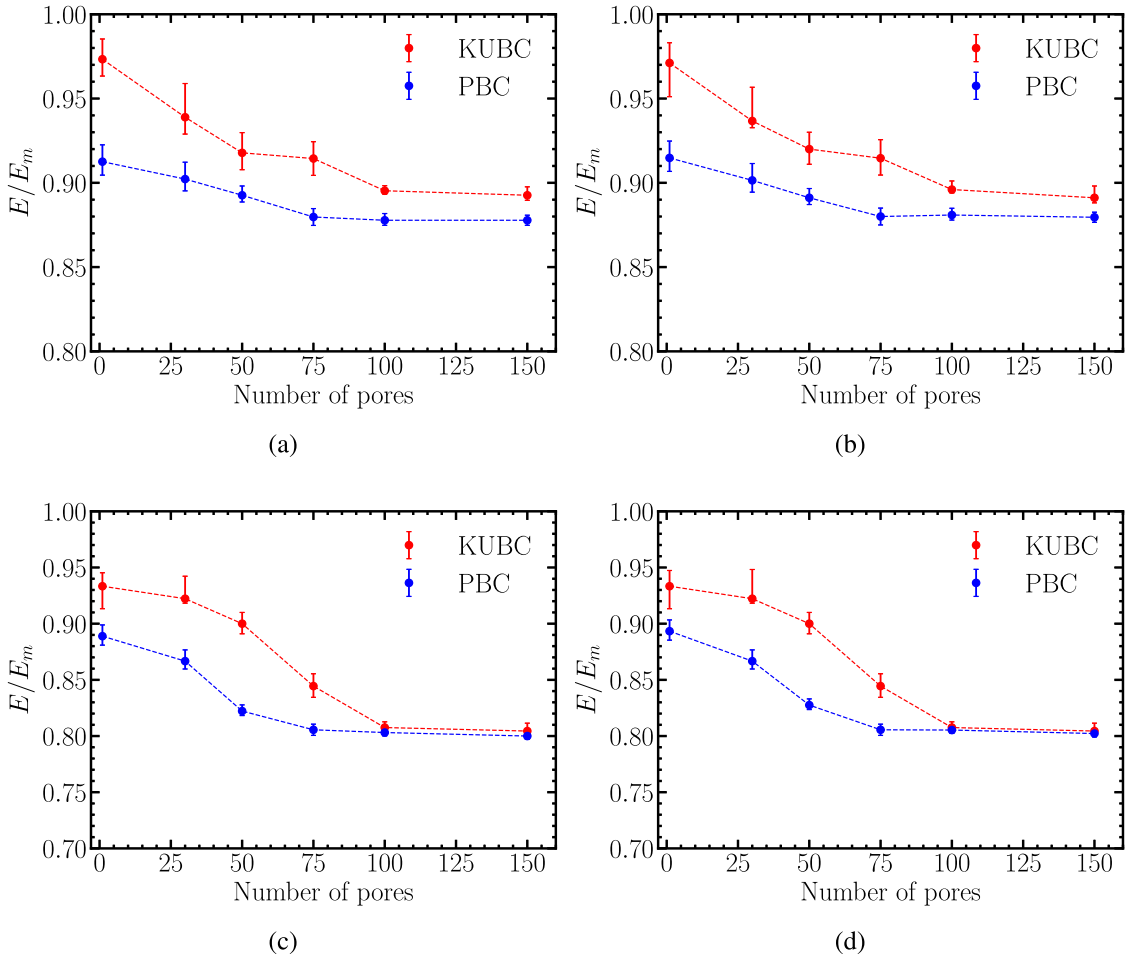

Fig. 6. Comparison between different sizes of unit cells for KUBC and PBC (a) f = 10vol% monodisperse microstructure, (b) f = 10vol% polydisperse microstructure, (c) f = 15vol% monodisperse microstructure and (d) f = 15vol% polydisperse microstructure. Normalised Young's modulus values are presented. The Young's moduli of the solid matrix is shown as E_m.

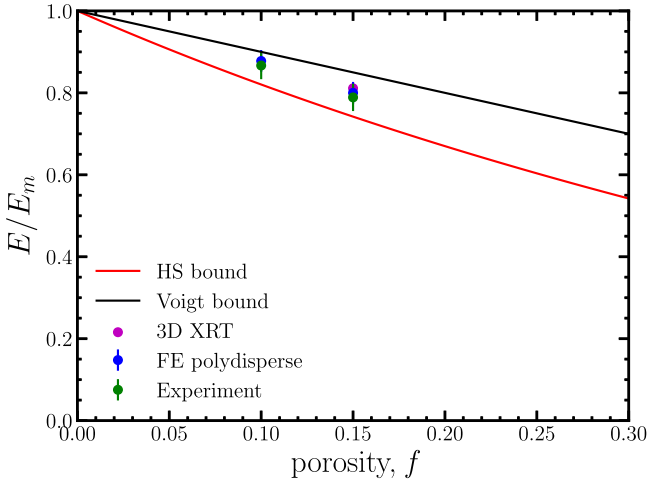

Fig. 7. Normalised Young's modulus calculated from experiments (Bikos et al., 2021b), micromechanical FE simulations using microstructures generated with the RSA algorithm and micromechanical FE simulations with the 3D XRT geometry for porosity f = 15vol%. The upper Hashin and Shtrikman and Voigt bounds are also shown.

(Fig. 9(a)) and monodisperse (Fig. 9(b)) distributions, whereas the softening starts in smaller strain values for the monodisperse unit cells, similar to Fig. 8. In tension, the polydisperse RVEs lie closer to the experimental data, whereas the monodisperse distribution does not provide a good prediction.

Table 4
Material properties for f = 10vol% and f = 15vol% micro-aerated chocolate for the FE simulations.

Parameter	f = 10vol%	f = 15vol%
Density, ρ [kg m^{-3}] (Bikos et al., 2021b)	1300	1300
Elastic modulus, E [MPa]	120	130
Poisson's ratio, ν [–]	0.49	0.49
A [MPa]	0.8	0.6
B [MPa]	2.1	1.7
C [–]	0.04	0.037
n [–]	0.7	0.63
$\dot{\varepsilon}_0$ [s^{-1}]	0.01	0.01
internal length, l [mm]	0.08	0.08
d_{cr}	0.1	0.1

Table 4 summarises the calibrated parameters of the constitutive and damage models for the two porosity levels. All the parameters were calibrated using the compression stress–strain curves. The tensile data were used for the estimation of the equivalent plastic strain at fracture initiation due to tension (Table 5).

Fig. 10(a) depicts the yield stress comparing experiments with monodisperse and polydisperse simulations for different strain rates for micro-aeration f = 10vol%. The yield stress is calculated as the first point when the linearity of the elastic region ends, following the methodology of Bikos et al. (2021b) to make possible the direct

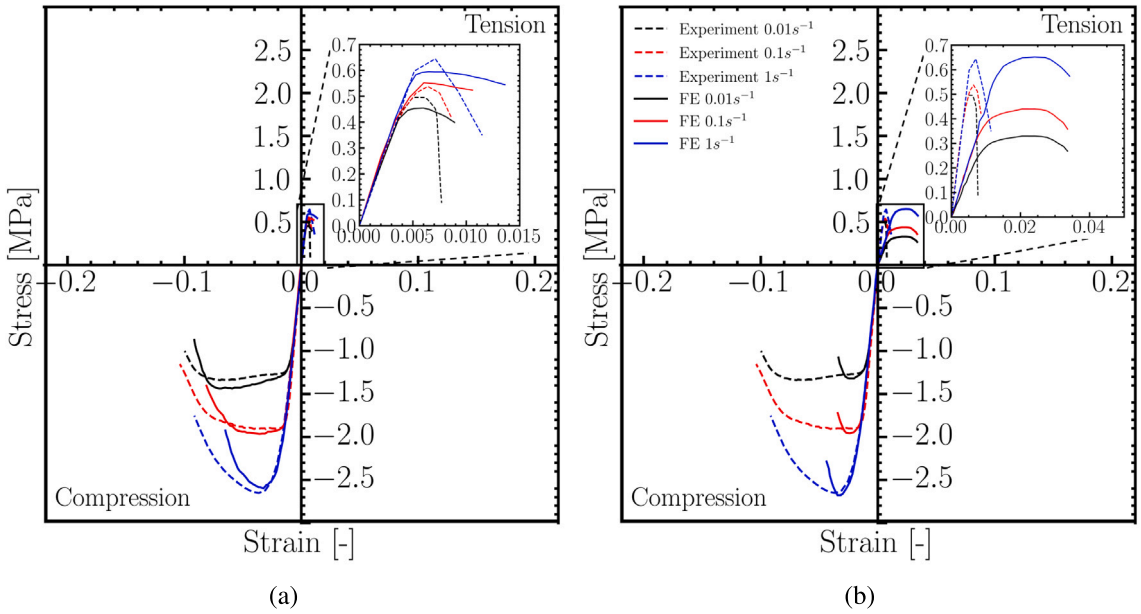

Fig. 8. Comparison between FE (solid lines) results and experimental results (dashed lines) for porosity f = 10vol% for different strain rates for (a) polydisperse and (b) monodisperse microstructure.

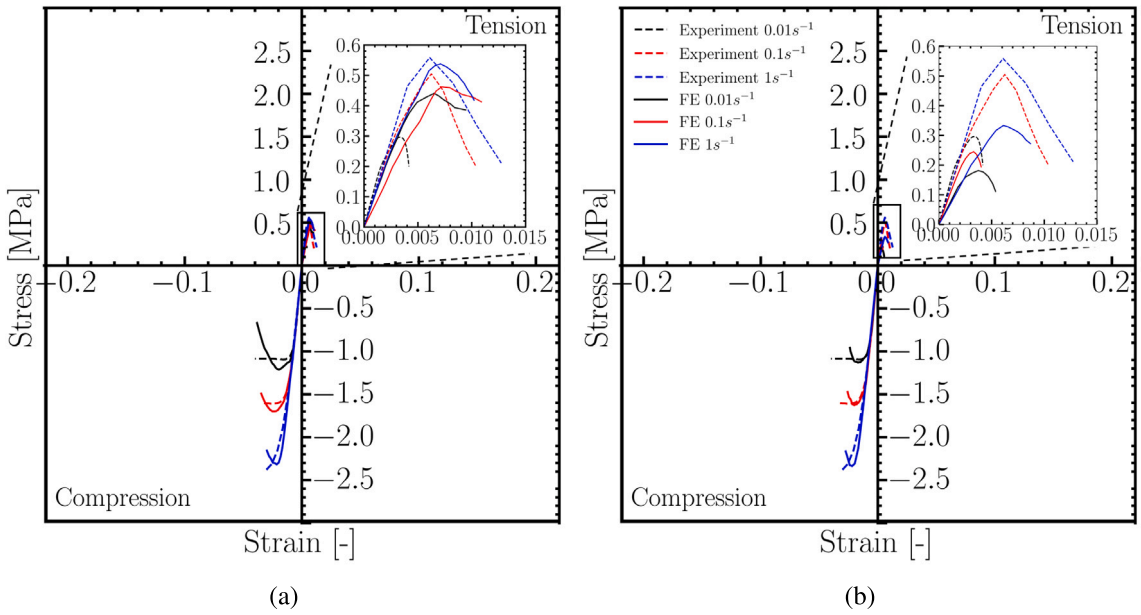

Fig. 9. Comparison between FE (solid lines) results and experimental results (dashed lines) for porosity f = 15vol% for different strain rates for (a) polydisperse and (b) monodisperse microstructure.

comparison between the FE calculations and the experimental results. Fig. 10(c) presents the equivalent plastic strain to failure for experiments and simulations in different strain rates for micro-aeration f = 10vol%. The respective data for the f = 15vol% porosity are presented in Figs. 10(b) and 10(d).

Another important aspect is the estimation of the equivalent plastic strain at the initiation of fracture of the micro aerated chocolate from the micromechanical simulations. The equivalent plastic strain at fracture initiation, $\varepsilon^p_{eq,i}$, is calculated from the strain that corresponds to the highest stress before softening. Then, the equivalent plastic strain is calculated through:

$$\varepsilon^p_{eq,i} = \varepsilon_{eq,i} - \frac{\sigma_{eq,i}}{E} \tag{16}$$

with the index i indicating the damage initiation and the values of $\varepsilon_{eq,i}$ and $\sigma_{eq,i}$ correspond to the highest stress value. Making use of Figs. 8(a) and 9(a) the equivalent plastic strain values at fracture initiation are calculated and the values are summarised in Table 5 for porosities f = 10vol% and f = 15vol% respectively. By using the relation $\varepsilon^p_{eq,s} = \frac{\sqrt{3}}{2}\varepsilon^p_{eq,t}$ for the equivalent plastic strain in shear the respective values for the equivalent plastic strain at the initiation of fracture were estimated.

5. Macro-mechanical simulation of the first bite

In this section, the *in silico* model for simulating the first bite will be presented. The micro-aerated chocolate samples are simulated as homogeneous using the material properties as those calculated from the micromechanical analysis of Section 4. Initially, the *in silico* FE model

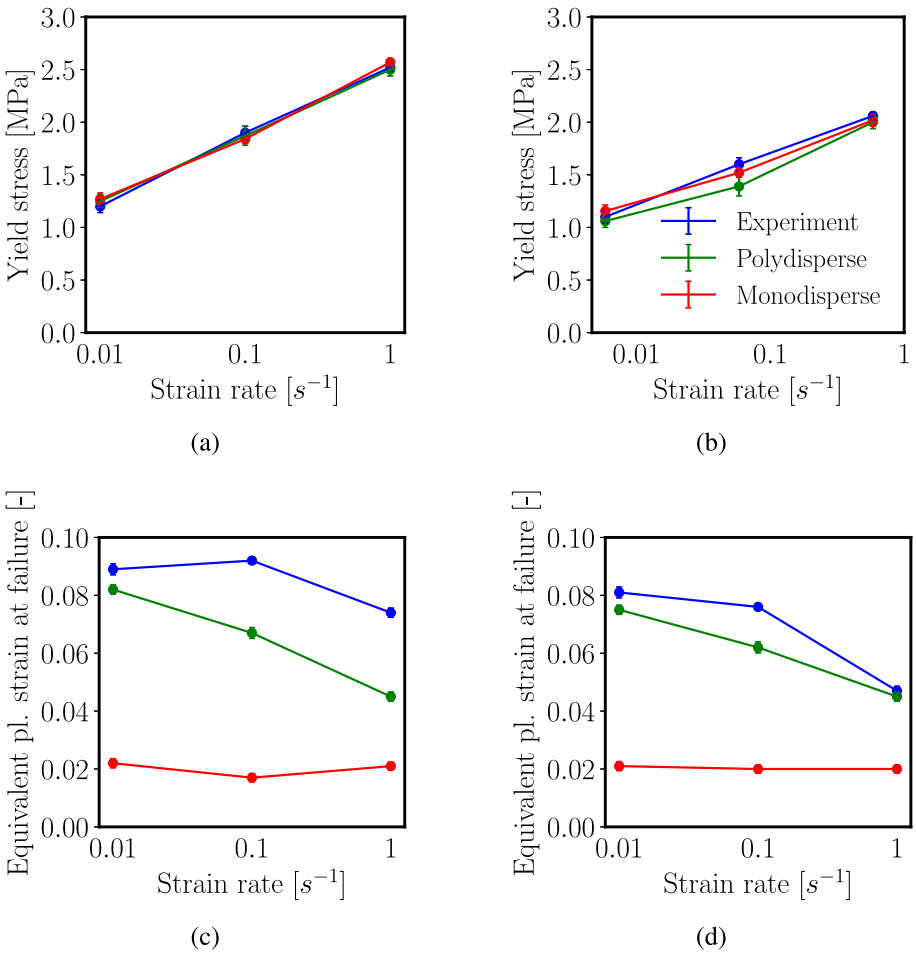

Fig. 10. Yield stress comparison between experimental data and FE results from polydisperse and monodisperse microstructures at different strain rates for porosity (a) f = 10vol% and (b) f = 15vol%. Plastic strain at failure comparison between experimental data and FE results from polydisperse and monodisperse microstructures in compression at different strain rates for porosity (c) f = 10vol% and (d) f = 15vol%.

Table 5
Equivalent plastic strain at damage onset for different stress states and strain rates for micro-aerated chocolate with porosity f = 10vol% and f = 15vol%.

	f = 10vol%		f = 15vol%	
η	$\varepsilon^p_{eq,i}$	$\dot{\varepsilon}(s^{-1})$	$\varepsilon^p_{eq,i}$	$\dot{\varepsilon}(s^{-1})$
−1/3	0.065	0.01	0.023	0.01
0	0.0048	0.01	0.0025	0.01
1/3	0.0055	0.01	0.003	0.01
−1/3	0.04	0.1	0.025	0.1
0	0.0052	0.1	0.0052	0.1
1/3	0.006	0.1	0.006	0.1
−1/3	0.03	1	0.03	1
0	0.0053	1	0.0044	1
1/3	0.0061	1	0.005	1

will be presented followed by the results and the fragmentation analysis were the results obtained by the *in vivo*, *in vitro* and *in silico* studies will be compared.

5.1. In silico model of the first bite

The geometry of the 3D printed pair of molar teeth was imported in ABAQUS via using discrete rigid surfaces for the teeth and a deformable part for the food specimen, according to the dimensions used in the experimental set-up (Fig. 11). The 3D printed teeth were considered as rigid, since the ABS is stiffer than the chocolate ($E_{ABS} \approx 1.9 - 2$ GPa > $E_{ch} \approx 0.1$ GPa (Meincke et al., 2004)). The chocolate specimens had dimensions 10×14×8 mm in order to be consistent with the experiment.

The Explicit solver of ABAQUS (Michael, 2017) was used for the FE models and the fully coupled thermal-stress analysis was run via a conventional personal computer (Intel(R) Core(TM) i7 7700K CPU 4.2 GHz). A semi-automatic mass scaling such that a maximum target time increment, $\Delta t = 10^{-5}$ s, is defined for the specified density, ρ = 1300 kg m^{-3}, while ensuring that the total kinetic energy is less than 2% of the total internal energy such that inertia effects are insignificant (Skamniotis et al., 2016). The upper and lower teeth were meshed with 23 742 four-node 3D bilinear rigid quadrilateral elements. The food specimen, with dimensions 10 mm×14 mm×8 mm, was meshed with 140 000 eight-node thermally coupled bricks, trilinear displacement and temperature elements (C3D8T) (Michael, 2017). A rigid surface was placed below the lower molar teeth and a gravitational force was applied to the food specimen after the completion of the first bite in order for the fragments to be removed from the teeth area. The size distribution of the fragments as they fell onto a flat plate due to gravity was measured using an identical methodology to that used for the in vivo mastication tests and the in vitro first bite tests in Section 2.4.

Another important aspect of the simulation is the friction coefficient between the teeth and the food specimen. Since, there is no available tribological experimental data between the ABS and the chocolate, a parametric study was conducted and a friction coefficient of μ = 0.8 for the non aerated chocolate captured well the force displacement experimental data (Samaras et al., 2023). The available tribological experimental results between tongue and palate, presented in Samaras

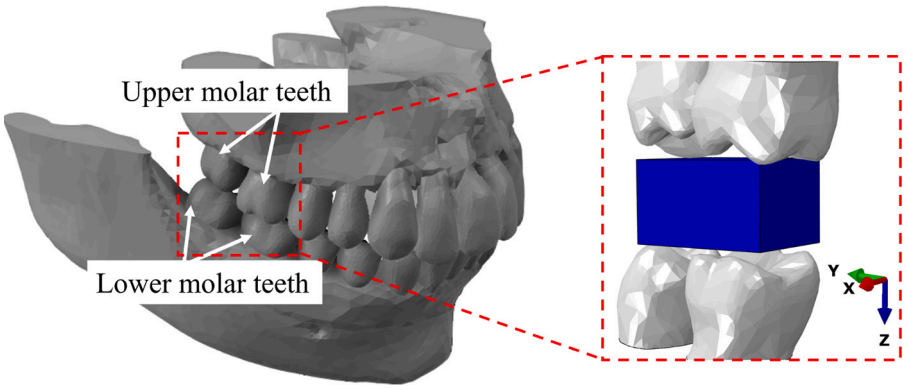

Fig. 11. The pair of molar teeth as those extracted and tilted from the full mouth geometry. The extracted molar teeth appear 180° rotated to be consistent with the experimental set-up.

et al. (2020), were used as a basis to estimate the decrease of the coefficient of friction due to micro-aeration between the micro-aerated samples and the teeth. The coefficient of friction values of $\mu_{10\%} = 0.33$ and $\mu_{15\%} = 0.2$ were measured for the $f = 10$vol% and $f = 15$vol% respectively, which was a 21% and 52% decrease comparing to the non aerated samples coefficient of friction, which was $\mu_{0\%} = 0.42$. The assumption that the coefficient of friction reduces due to micro-aeration by the same percentage as the tribological experiments indicated was made. Following this rationale, for the $f = 10$vol% micro-aerated chocolate a coefficient of friction $\mu_{10\%} = 0.63$ was applied. This value was selected considering the 21% decrease, compared to the non-aerated samples, captured by the tribological experiments. The coefficient of friction between the 3D printed teeth and the $f = 15$vol% micro-aerated chocolate was selected as $\mu_{15\%} = 0.38$, which is a 52% reduction compared to the non aerated coefficient of friction value. All the first bite simulations were run at a chewing speed of $\dot{\delta} = 15\,\text{mm}\,\text{s}^{-1}$ which is closer to the physiological conditions in the mouth (Bikos et al., 2021b).

5.2. Effect of micro-aeration on the first bite

The force–displacement results from the *in vitro* and *in silico* studies for the non aerated, $f = 10$vol% and $f = 15$vol% micro-aerated samples are shown in Fig. 12. The value of $l_{ch} = 0.1\,\text{mm}$ provided mesh independent results for the *in silico* model as shown in the study of Samaras et al. (2023). Both *in vitro* and *in silico* results are plotted for a speed $\dot{\delta} = 15\,\text{mm}\,\text{s}^{-1}$. The micro-aerated samples were considered as homogeneous with the mechanical properties as those calculated from the micromechanical analysis presented in Section 4 and are summarised in Tables 2 and Table 4. The error bars in Fig. 12 correspond to five different placements of the chocolate relative to the teeth in both experiments and simulations and represent the minimum and maximum values. There is a good agreement between *in silico* and *in vitro* data for all micro-aeration levels.

5.3. Analysis of fragmentation results

Fig. 13(a) shows the fragments as those collected after the *in vitro* experiment. Similar fragmentation images were obtained from the *in vivo* and the *in silico* FE model. The images were then turned into 8-bit format (black and white), as shown in Fig. 13(b). Figs. 14(a) and 14(b) depict the particle size distributions obtained from the *in vivo*, *in silico* and *in vitro* non-aerated and $f = 15$vol% micro-aerated specimens respectively. The blue *in vivo* scatter points are acquired from the study of Bikos et al. (2021b) and are compared with the *in vitro* experimental results and the *in silico* model at a chewing speed of $\dot{\delta} = 15\,\text{mm}\,\text{s}^{-1}$ obtained from this study, since it is closer to the physiological conditions in the mouth. During the first bite, over 76%

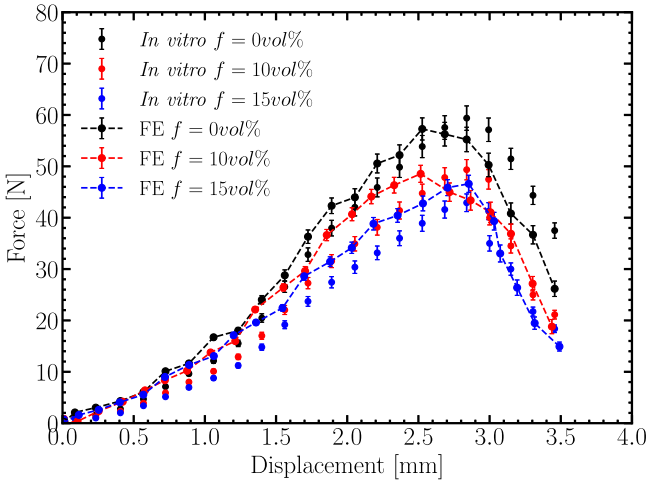

Fig. 12. Comparison between *in vitro* experimental and FE force displacement data for the non-aerated, $f = 10$vol% and $f = 15$vol% micro-aerated chocolate. All values correspond to a speed of $\dot{\delta} = 15\,\text{mm}\,\text{s}^{-1}$.

of the non-aerated fragments are smaller than 1.25 mm, compared to the respective value of 88% for $f = 15$vol% micro-aerated samples. At this point, it is worth noting that the $f = 10$vol% chocolate samples were not included in the fragmentation study, since *in vivo* fragmentation results were not available for this porosity.

The error bars of the *in silico* model, correspond to the maximum and minimum value of five simulations where the relative position between the teeth and the sample was changed randomly. The same procedure was followed for the *in vitro* data were acquired from five repeats. The FE *in silico* model lies in good agreement with both the *in vivo* and *in vitro results*.

6. Discussion

Our work aims at estimating the effect that micro-aeration has on the mechanical properties of chocolate and use these findings to investigate the effect of micro-aeration on the mechanical breakdown of chocolate during the first bite. In the past, a plethora of studies have investigated the mechanical breakdown of foods during mastication in order to provide a reliable simulation tool e.g. Harrison et al. (2014), Harrison and Cleary (2014), Skamniotis et al. (2019). A key improvement of the current study is the multiscale analysis that is conducted starting from the microscale and applying the estimated mechanical properties in the macroscale first bite FE simulations. In addition, a more advanced non local damage model was used to reduce mesh

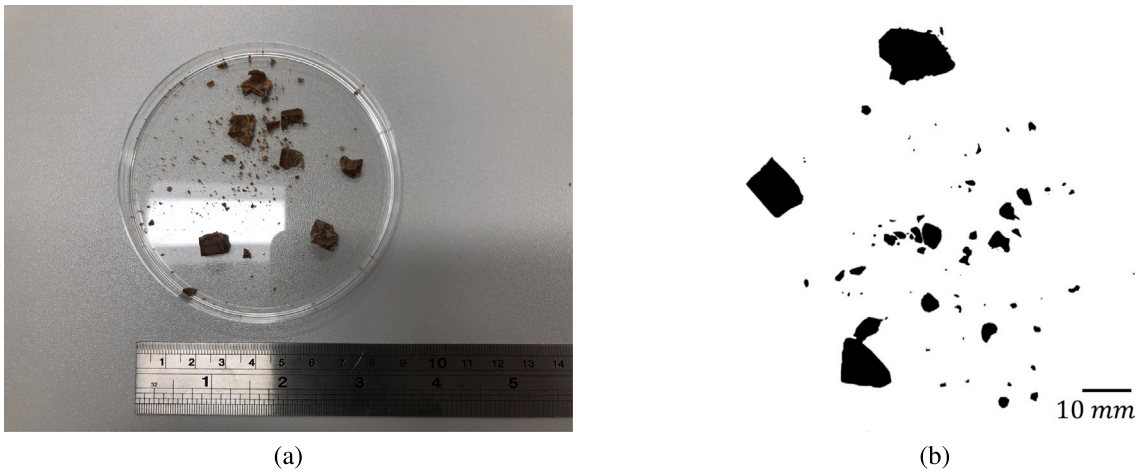

Fig. 13. (a) Representative example of chocolate fragments after the *in vitro* tests of non-aerated samples was examined; similar fragments are obtained from the *in vivo* tests, (b) binary image used to calculate the size distribution of the fragments.

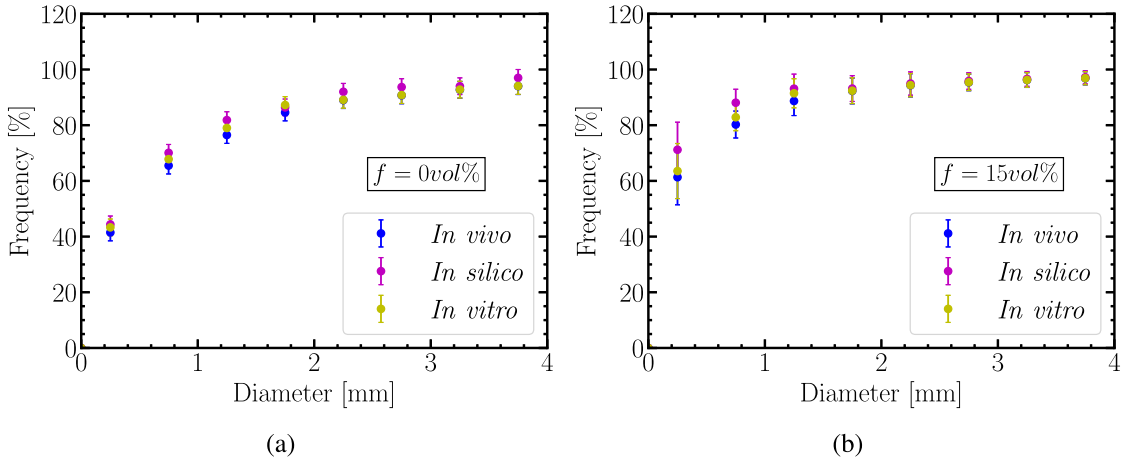

Fig. 14. Comparison of fragment diameter between *in vitro*, *in silico* and *in vivo* mastication tests conducted for (a) non-aerated samples and (b) $f = 15\text{vol}\%$ micro-aerated samples. The *in vivo* results were obtained from the study of Bikos et al. (2021b).

dependency of the simulations. This work combined with our previous publications in the field provides a computational and experimental methodology that takes into account microstructural changes (micro-aeration) and provides results on the macroscale (fragmentation during the first bite).

An assumption made in the current study is that the solid matrix of the micro-aerated samples has the same properties as the non aerated samples. For this reason, the l_{ch} parameter remains constant, at 60 μm, for all micro-aeration levels, since it can be related to the sugar crystal size, which lies in the same length scale (10–40 μm) and is present in both micro-aerated and non aerated chocolate. This assumption might be the reason for the differences that are present between the FE results and the experimental data presented in Figs. 10c and 10d. Another reason for underestimating the fracture strain in Figs. 10c and 10d is the fact that the matrix is considered as homogeneous without taking into account other constituents that are present in the chocolate matrix e.g. sugar crystals. This addition could provide more accurate results but would also require properties of all the constituents and their interfaces. In addition, the damage model parameters l and d_{cr} remained constant across the different micro-aeration levels as it was found to agree well with the experimental data.

The study of the fragment size distribution revealed a clear difference between the non aerated and micro-aerated chocolate. Based on Figs. 14(a) and 14(b), it is evident that the micro-aerated chocolate specimens break into more smaller pieces comparing to the non-aerated samples, implying that the fragmentation is aided by micro-aeration. This difference is also aligned with the findings from the micromechanical analysis, where a decrease of the fracture strain was observed with increasing micro-aeration level, shown in Tables 3 for the micro-aerated chocolate and Table 5 for the two porosity levels.

The degradation of the mechanical properties, due to micro-aeration, as those measured by experiments (Bikos et al., 2021b) and validated through the computational models, showed that micro-aeration decreases the Young's modulus, and the fracture strain. These mechanical properties can be linked to the textural properties such as softness, hardness and crumbliness which are present at the early stages of the oral processing. The increase of fragmentation between the two types of chocolate can potentially influence the melting time of the fragments, since more surface is exposed to the mouth temperature and the saliva. The reduced melting time can aid the thin film formation in the mouth surfaces, which is related to the tribological properties and it is in agreement with the tribological findings of Samaras et al. (2020). A detailed analysis and link between chocolate structure, material properties and sensory perception was presented in the study of Bikos et al. (2022a). Although micro-aerated samples had less sugar content, the sweetness remained at the same level according to the sensory panel test. This was also validated from our fragmentation analysis where the smaller-sized fragments of the $f = 15\text{vol}\%$, allow for more surface to be exposed to the mouth temperature and therefore accelerate melting. According to Bikos et al. (2022a) the faster melting time can be

associated with increased sweetness perception. Based on the sensory tests, structural changes can create significant changes in the sensorial profile and the evolution of sensorial attributes during oral processing. It is believed that there is a connection between structure and sensorial attributes, but there is the need for conclusive statistical analysis to validate those findings (Bikos et al., 2022a). Our work shows that it is possible to make new food structures associated with favourable outcomes in both consumer perception and human health.

7. Conclusions

Our study provides a multiscale framework that quantifies the effect of micro-aeration on the mechanical properties of chocolate and subsequently how the first bite is influenced by this micromechanical change.

We conducted a micromechanical computational study in order to estimate the effect that micro-aeration has on the mechanical properties. A unit cell with 100 pores was considered as representative of the entire volume and was used for the simulations. In compression, the predicted Young's modulus was found to agree well with the experimental data for both micro-aeration levels $f = 10$vol% and $f = 15$vol% for both monodisperse and polydisperse pore diameter distributions. The same RVEs were used for the estimation of the plastic and fracture properties. In both examined porosities the yield point in compression was found to be in good agreement with the experimental data for both monodisperse and polydisperse microstructures. However, only the polydisperse RVEs predicted well the strain at failure. The unit cells were also subjected to tension and the polydisperse RVEs were found to lie closer to the experimental data, whereas the monodisperse distribution did not provide a good prediction. The data from the tension results were used to estimate the equivalent plastic strain at fracture initiation due to tension. The estimated elastic, plastic and fracture properties were used in the macroscopic *in silico* simulations of the first bite. A digitised adult male 3D skull, generated using X-ray computed tomography, was used to extract a pair of the two last molar teeth for the *in silico* simulations and the same pair of molar teeth was 3D printed for the experimental *in vitro* set-up. The force–displacement curves from the *in silico* simulations were found to agree well with the *in vitro* experimental data for the non-aerated chocolate and for both micro-aeration levels. Furthermore, the analysis conducted using the chocolate fragments as derived from the *in vivo*, *in vitro* and *in silico* showed a good agreement and captured the difference in fragmentation size due to micro-aeration between the non-aerated and the $f = 15$vol% micro-aerated chocolate.

The presented combined modelling and experimental methodology enables cost and time-efficient design tools for new food structures that will contribute to developing food products with lower calorific value while improving the consumer perception. This study combined with already published work from our group (Bikos et al., 2021b,a, 2022b; Samaras et al., 2020; Bikos et al., 2023a, 2022a) can be used towards designing an optimised food structure that enhances the mechanical, thermal and tribological properties of foods, while simultaneously decreasing the calorific value and providing an overall nutritionally superior end product.

CRediT authorship contribution statement

Georgios Samaras: Conceptualization, Data curation, Investigation, Writing – original draft, Writing – review & editing. **Dimitrios Bikos:** Conceptualization, Writing – review & editing. **Philippa Cann:** Conceptualization, Writing – review & editing. **Marc Masen:** Conceptualization, Writing – review & editing. **Yannis Hardalupas:** Conceptualization, Writing – review & editing. **Josélio Vieira:** Conceptualization, Writing – review & editing. **Christoph Hartmann:** Conceptualization, Writing – review & editing. **Maria Charalambides:** Conceptualization, Project administration, Supervision, Writing – original draft, Writing – review & editing.

Declaration of competing interest

The authors declare the following financial interests/personal relationships which may be considered as potential competing interests: Dimitrios Bikos reports financial support was provided by Nestlé Research Center.

Data availability

Data will be made available on request.

Acknowledgments

The authors would like to acknowledge Imperial College President's PhD scholarship and the Engineering and Physical Sciences Research Council (EPSRC) for the financial support. This work was also supported by the Centre for Doctoral Training on Theory and Simulation of Materials (CDT-TSM) at Imperial College London. Moreover, the authors acknowledge the Nestlé PTC York for funding the project and providing the materials for testing.

References

Afoakwa, E.O., Paterson, A., Fowler, M., Vieira, J., 2009. Microstructure and mechanical properties related to particle size distribution and composition in dark chocolate. Int. J. Food Sci. Technol. 44 (1), 111–119.
Aifantis, E.C., 1984a. On the microstructural origin of certain inelastic models. J. Eng. Mater. Technol. Trans. ASME 106 (4), 326–330.
Aifantis, E.C., 1984b. On the microstructural origin of certain inelastic models. J. Eng. Mater. Technol. 106 (4), 326–330.
Anoukou, K., Brenner, R., Hong, F., Pellerin, M., Danas, K., 2018. Random distribution of polydisperse ellipsoidal inclusions and homogenization estimates for porous elastic materials. Comput. Struct. 210, 87–101.
Aravas, N., Papadioti, I., 2021. A non-local plasticity model for porous metals with deformation-induced anisotropy: Mathematical and computational issues. J. Mech. Phys. Solids 146, 104190.
Bai, Y., Wierzbicki, T., 2008. A new model of metal plasticity and fracture with pressure and lode dependence. Int. J. Plast. 24 (6), 1071–1096.
Bikos, D., 2022. Effect of micro-aeration on mechanical and thermal properties of chocolate and correlation to oral processing (Ph.D. thesis). Imperial College London.
Bikos, D., Samaras, G., Cann, P., Masen, M., Hardalupas, Y., Charalambides, M.N., Hartmann, C., German, J., Vieira, J., 2021a. Effect of structure on the mechanical and physical properties of chocolate considering time scale phenomena occurring during oral processing. Food Struct. 31, 100244.
Bikos, D., Samaras, G., Cann, P., Masen, M., Hardalupas, Y., Charalambides, M.N., Hartmann, C., German, J., Vieira, J., 2022a. Effect of structure on the mechanical and physical properties of chocolate considering time scale phenomena occurring during oral processing. Food Struct. 31, 100244.
Bikos, D., Samaras, G., Cann, P., Masen, M., Hardalupas, Y., Hartmann, C., Vieira, J., Charalambides, M.N., 2021b. Effect of micro-aeration on the mechanical behaviour of chocolates and implications for oral processing. Food Funct. 12 (11), 4864.
Bikos, D., Samaras, G., Cann, P., Masen, M., Hardalupas, Y., Vieira, J., Hartmann, C., Huthwaite, P., Lan, B., Charalambides, M.N., 2023a. Destructive and non-destructive mechanical characterisation of chocolate with different levels of porosity under various modes of deformation. J. Mater. Sci. 58, 5104–5127.
Bikos, D., Samaras, G., Charalambides, M.N., Cann, P., Masen, M., Hartmann, C., Vieira, J., Sergis, A., Hardalupas, Y., 2022b. Experimental and numerical evaluation of the effect of micro-aeration on the thermal properties of chocolate. Food Funct. 13 (9), 4993–5010.
Bikos, D., Samaras, G., Charalambides, M.N., Cann, P., Masen, M., Hartmann, C., Vieira, J., Sergis, A., Hardalupas, Y., 2023b. A micromechanical based finite element model approach to accurately predict the effective thermal properties of micro-aerated chocolate. Innov. Food Sci. Emerg. Technol. 83, 103227.
Castañeda, P.P., 1991. The effective mechanical properties of nonlinear isotropic composites. J. Mech. Phys. Solids 39 (1), 45–71.
Castaneda, P.P., 2002. Second-order homogenization estimates for nonlinear composites incorporating field fluctuations: I-theory. J. Mech. Phys. Solids 50 (4), 737–757.
Chen, J., 2009. Food oral processing—A review. Food Hydrocolloids 23 (1), 1–25.
Cheong, J.N., Foster, K.D., Morgenstern, M.P., Grigor, J.M.V., Bronlund, J.E., Hutchings, S.C., Hedderley, D.I., 2014. The application of temporal dominance of sensations (TDS) for oral processing studies: An initial investigation. J. Texture Stud. 45 (6), 409–419.
Dejak, B., Młotkowski, A., Romanowicz, M., 2003. Finite element analysis of stresses in molars during clenching and mastication. J. Prosthet. Dent. 90 (6), 591–597.
Di Monaco, R., Su, C., Masi, P., Cavella, S., 2014. Temporal dominance of sensations: A review. Trends Food Sci. Technol. 38 (2), 104–112.

Do, T., Hargreaves, J.M., Wolf, B., Hort, J., Mitchell, J.R., 2007. Impact of particle size distribution on rheological and textural properties of chocolate models with reduced fat content. J. Food Sci. 72 (9), E541–E552.
Dorgan, R.J., 2006. A Nonlocal Model for Coupled Damage-Plasticity Incorporating Gradients of Internal State Variables At Multiscales. Louisiana State University and Agricultural & Mechanical College.
Enakoutsa, K., 2014. An improved nonlocal gurson model for plastic porous solids, with an application to the simulation of ductile rupture tests. Appl. Math. Model. 38 (11–12), 2791–2799.
Glicerina, V., Balestra, F., Dalla Rosa, M., Romani, S., 2016. Microstructural and rheological characteristics of dark, milk and white chocolate: A comparative study. J. Food Eng. 169, 165–171.
Harrison, S.M., Cleary, P.W., 2014. Towards modelling of fluid flow and food breakage by the teeth in the oral cavity using smoothed particle hydrodynamics (SPH). Eur. Food Res. Technol. 238 (2), 185–215.
Harrison, S.M., Eyres, G., Cleary, P.W., Sinnott, M.D., Delahunty, C., Lundin, L., 2014. Computational modeling of food oral breakdown using smoothed particle hydrodynamics. J. Texture Stud. 45 (2), 97–109.
Hashin, Z., Shtrikman, S., 1963. A variational approach to the theory of the elastic behaviour of multiphase materials. J. Mech. Phys. Solids 11 (2), 127–140.
Huet, C., 1990. Application of variational concepts to size effects in elastic heterogeneous bodies. J. Mech. Phys. Solids 38 (6), 813–841.
Huet, C., 1999. Coupled size and boundary-condition effects in viscoelastic heterogeneous and composite bodies. Mech. Mater. 31 (12), 787–829.
Jackiewicz, J., Kuna, M., 2003. Non-local regularization for FE simulation of damage in ductile materials. Comput. Mater. Sci. 28 (3–4), 684–695.
Kanit, T., Forest, S., Galliet, I., Mounoury, V., Jeulin, D., 2003. Determination of the size of the representative volume element for random composites: Statistical and numerical approach. Int. J. Solids Struct. 40 (13–14), 3647–3679.
Kokini, J., van Aken, G., 2006. Discussion session on food emulsions and foams. Food Hydrocolloids 20 (4), 438–445.
Le, D.T., Marigo, J., Maurini, C., Vidoli, S., 2018. Strain-gradient vs damage-gradient regularizations of softening damage models. Comput. Methods Appl. Mech. Engrg. 340, 424–450.
Leblond, J.B., Perrin, G., Devaux, J., 1994. Bifurcation effects in ductile metals with nonlocal damage.
Lucas, P.W., Luke, D.A., 1983. Methods for analysing the breakdown of food in human mastication. Arch. Oral Biol. 28 (9), 813–819.
Mbiakop, A., Constantinescu, A., Danas, K., 2015. An analytical model for porous single crystals with ellipsoidal voids. J. Mech. Phys. Solids 84, 436–467.
Meincke, O., Kaempfer, D., Weickmann, H., Friedrich, C., Vathauer, M., Warth, H., 2004. Mechanical properties and electrical conductivity of carbon-nanotube filled polyamide-6 and its blends with acrylonitrile/butadiene/styrene. Polymer 45 (3), 739–748.
Michael, S., 2017. ABAQUS/Standard User's Manual, Version 6.17. Dassault Systèmes Simulia Corp, United States.
Michel, J.C., Suquet, P., 1992. The constitutive law of nonlinear viscous and porous materials. J. Mech. Phys. Solids 40 (4), 783–812.
Minor, M., Vingerhoeds, M.H., Zoet, F.D., De Wijk, R., Van Aken, G.A., 2009. Preparation and sensory perception of fat-free foams–effect of matrix properties and level of aeration. Int. J. Food Sci. Technol. 44 (4), 735–747.
Ostoja-Starzewski, M., 1998. Random field models of heterogeneous materials. Int. J. Solids Struct. 35 (19), 2429–2455.
Ostoja-Starzewski, M., 1999. Scale effects in materials with random distributions of needles and cracks. Mech. Mater. 31 (12), 883–893.
Papadioti, I., Aravas, N., Lian, J., Münstermann, S., 2019. A strain-gradient isotropic elastoplastic damage model with J3 dependence. Int. J. Solids Struct. 174, 98–127.
Pecullan, S., Gibiansky, L.V., Torquato, S., 1999. Scale effects on the elastic behavior of periodic andhierarchical two-dimensional composites. J. Mech. Phys. Solids 47 (7), 1509–1542.
Peerlings, R.H.J., de Borst, R., Brekelmans, W.A.M., De Vree, J.H.P., 1996. Gradient enhanced damage for quasi-brittle materials. Int. J. Num. Methods Eng. 39 (19), 3391–3403.
Pijaudier-Cabot, G., Bažant, Z.P., 1987. Nonlocal damage theory. J. Eng. Mech. 113 (10), 1512–1533.
Reinke, S.K., Wilde, F., Kozhar, S., Beckmann, F., Vieira, J., Heinrich, S., Palzer, S., 2016. Synchrotron X-Ray microtomography reveals interior microstructure of multicomponent food materials such as chocolate. J. Food Eng. 174, 37–46.
Reusch, F., Svendsen, B., Klingbeil, D., 2003. A non-local extension of gurson-based ductile damage modeling. Comput. Mater. Sci. 26, 219–229.
Richter, H., 2017. Mote3D: An open-source toolbox for modelling periodic random particulate microstructures. Modelling Simul. Mater. Sci. Eng. 25 (3).
Rintoul, M.D., Torquato, S., 1997. Reconstruction of the structure of dispersions. J. Colloid Interface Sci. 186 (2), 467–476.
Sahagian, D.L., Proussevitch, A.A., 1998. 3D particle size distributions from 2D observations: Stereology for natural applications. J. Volcanol. Geotherm. Res. 84 (3–4), 173–196.
Samaras, G., Bikos, D., Skamniotis, C., Cann, P., Masen, M., Hardalupas, Y., Vieira, J., Hartmann, C., Charalambides, M., 2023. Experimental and computational models for simulating the oral breakdown of food due to the interaction with molar teeth during the first bite. Extreme Mech. Lett. 102047.
Samaras, G., Bikos, D., Vieira, J., Hartmann, C., Charalambides, M., Hardalupas, Y., Masen, M., Cann, P., 2020. Measurement of molten chocolate friction under simulated tongue-palate kinematics: Effect of cocoa solids content and aeration. Curr. Res. Food Sci. 3, 304–313.
Schneider, C.A., Rasband, W.S., Eliceiri, K.W., 2012. NIH image to ImageJ: 25 years of image analysis. Nat. Methods 9 (7), 671–675.
Schöberl, J., 1997. An advancing front 2D/3D-mesh generator based on abstract rules. Comput. Vis. Sci. 1 (1), 41–52.
Seupel, A., Hütter, G., Kuna, M., 2018. An efficient FE-implementation of implicit gradient-enhanced damage models to simulate ductile failure. Eng. Fract. Mech. 199, 41–60.
Skamniotis, C.G., Elliott, M., Charalambides, M.N., 2017. On modeling the large strain fracture behaviour of soft viscous foods. Phys. Fluids 29 (12), 121610.
Skamniotis, C., Elliott, M., Charalambides, M.N., 2019. On modelling the constitutive and damage behaviour of highly non-linear bio-composites–mesh sensitivity of the viscoplastic-damage law computations. Int. J. Plast. 114, 40–62.
Skamniotis, C., Patel, Y., Charalambides, M.N., Elliott, M., 2016. Fracture investigation in starch-based foods. Interface Focus 6 (3).
Terada, K., Hori, M., Kyoya, T., Kikuchi, N., 2000. Simulation of the multi-scale convergence in computational homogenization approaches. Int. J. Solids Struct. 37 (16), 2285–2311.
Wan, W., Yang, J., Xu, G., Liu, Y., 2021. Determination and evaluation of Holmquist-Johnson-Cook constitutive model parameters for ultra-high-performance concrete with steel fibers. Int. J. Impact Eng. 156, 103966.
Wu, B., Li, X., Di, Y., Brinnel, V., Lian, J., Münstermann, S., 2017. Extension of the modified Bai-Wierzbicki model for predicting ductile fracture under complex loading conditions. Fatigue Fract. Eng. Mater. Struct. 40 (12), 2152–2168.
Yven, C., Guessasma, S., Chaunier, L., Della Valle, G., Salles, C., 2010. The role of mechanical properties of brittle airy foods on the masticatory performance. J. Food Eng. 101 (1), 85–91.
Zerhouni, O., Tarantino, M.G., Danas, K., 2019. Numerically-aided 3D printed random isotropic porous materials approaching the Hashin-Shtrikman bounds. Composites B 156, 344–354.